mater.scichina.com link.springer.com

Published online 4 March 2022 | https://doi.org/10.1007/s40843-021-1944-9
Sci China Mater 2022, 65(7): 1797–1804

Coherent V^{4+}-rich V_2O_5/carbon aerogel nanocomposites for high performance supercapacitors

Wenchao Bi[1,2,3], Shengyuan Deng[2], Haisha Tang[1], Yuan Liu[1], Jun Shen[2], Guohua Gao[2*], Guangming Wu[2*], M. Atif[4,5], MS AlSalhi[4,5] and Guozhong Cao[3*]

ABSTRACT **V^{4+}-rich V_2O_5/carbon aerogel (V^{4+}-V_2O_5/CA) composites were synthesized as electrode materials for supercapacitors *via in-situ* hydrolysis-condensation processing. Carbon aerogel (CA) promotes the deposition of amorphous vanadium oxide and catalyzes the crystallization of V^{4+}-rich V_2O_5 nanosheets at much reduced temperature. With a uniform distribution of V_2O_5 nanosheets in CA, the special structure provides a large specific area and reactive sites. CA also synergistically improves the electrical conductivity and structural integrity. In addition, rich V^{4+} would enhance the intrinsic electrical conductivity of V_2O_5, promote ion diffusion and catalyze the electrochemical reactions. Consequently, V^{4+}-V_2O_5/CA exhibits much enhanced specific capacitance (405 F g^{-1} at 0.5 A g^{-1}), high energy density (56 W h kg^{-1} with a power density of 250 W kg^{-1}) and long cycle life (96% capacitance retention after 40,000 cycles).**

Keywords: V_2O_5, V^{4+}, carbon aerogel, kinetics, supercapacitor

INTRODUCTION

Efficient energy storage devices are crucial for applying intermittent renewable energy sources, such as solar, hydro, and wind energy [1]. Supercapacitors deliver short charging time, high power densities and ultralong cycle life [2–4] and thus have been applied in many fields, including portable electronic products, hybrid electric vehicles and so on [5–7]. However, the commercially available supercapacitors show much lower energy density (~5 W h kg^{-1}) than batteries (up to 200 W h kg^{-1}) [5]. More research efforts are made to achieve high energy-storage capability. Energy density (E) can be achieved by improving the specific capacitance (C) of electrode materials and enlarging the voltage window (ΔV) according to $E = (1/2)C(\Delta V)^2$ [8,9]. Pseudocapacitors, one kind of supercapacitors which store charges by fast, reversible Faradic redox reactions of conducting polymers, transition metal oxides, metal carbides, metal sulfides and so on, can deliver high theoretical specific capacitance but unsatisfactory stability. Electrochemical double layer capacitors (EDLCs) are another kind of supercapacitors based on carbonaceous materials, and possess excellent stability due to the electrostatic adsorption/desorption of charges [2,10]. Thus, optimized electrode materials with expected electrochemical properties are important for high-energy-density supercapacitors [9–12].

Carbonaceous materials (such as graphene, carbon nanotubes and porous carbon materials) are widely used in EDLCs for their high electrical conductivity, excellent structural stability and long cycle life [13–16]. Among them, carbon aerogels (CA) derived from organic hydrogels with polycondensation of resorcinol and formaldehyde [17] were explored in EDLCs for inherent characteristics, including tunable porous structure, large specific area, scalable preparation, and low cost. However, the specific capacitance of CA supercapacitors is usually less satisfactory due to its intrinsic limitation of electric double layer storage mechanism.

Transition metal oxides, on the other hand, offer far large capacities through electrochemical reactions; for example, vanadium pentoxide (V_2O_5) shows high theoretical capacitance (2020 F g^{-1}) derived from multiple states (+2–+5) [18–20], but suffers from low electrical conductivity and poor cycling stability. To improve the performance, nanostructured V_2O_5-based materials with various morphologies, sizes and shapes, including nanowires [21], nanotubes [22], nanobelts [23], nanoribbons [24] and nanoporous network [25], were investigated. Incorporating vanadium oxides with highly conductive carbonaceous materials is a feasible strategy to achieve high electrochemical performance and stability. For instance, efficient redox activity and high conductivity were demonstrated in V_2O_5/carbon composite due to the synergistic effects of V_2O_5 and porous carbon [26]. V^{4+} can also promote ion diffusion kinetics, enhance electrical conductivity and improve storage capacity of V_2O_5 [27].

In this study, V^{4+}-rich V_2O_5 and CA (noted as V^{4+}-V_2O_5/CA) composites were fabricated and studied for supercapacitors. A functionalized VO_x sol was hydrolyzed and condensed in CA when exposed in water vapor. V_2O_5 nanosheets rich with V^{4+} were uniformly distributed in CA. Due to the synergistic integration of porous nanostructure of CA and V^{4+}-rich V_2O_5 nanosheets, great electrochemical performance of V^{4+}-V_2O_5/CA was achieved (405 F g^{-1} at 0.5 A g^{-1}) with excellent cycling stability. The transport and reaction kinetics and structural integration were discussed.

[1] Departments of Physics, College of Science, University of Shanghai for Science and Technology, Shanghai 200093, China
[2] Shanghai Key Laboratory of Special Artificial Microstructure, School of Physics Science and Engineering, Tongji University, Shanghai 200092, China
[3] Department of Materials Science and Engineering, University of Washington, Seattle, WA 98195-2120, United States
[4] Research Chair on Laser Diagnosis of Cancers, Department of Physics and Astronomy, College of Science, King Saud University, 11451, Riyadh, Saudi Arabia
[5] Department of Physics and Astronomy, College of Science, King Saud University, 11451, Riyadh, Saudi Arabia
[*] Corresponding authors (emails: gao@tongji.edu.cn (Gao G); wugm@tongji.edu.cn (Wu G); gzcao@u.washington.edu (Cao G))

EXPERIMENTAL SECTION

Fabrication of V^{4+}-V_2O_5/CA nanocomposite

CA was prepared with resorcinol and formaldehyde as raw materials according to a reported method [17]. VO_x sol was prepared by continuously stirring a mixture of commercial V_2O_5 powder, benzyl alcohol and isopropanol (a molar ratio of 1:4:40) at 90°C for 4 h, and then condensing the clear solution to 1/3 volume [28]. The synthesis of V^{4+}-V_2O_5/CA was schematically illustrated in Fig. 1a. Firstly, the as-prepared CA was immersed into a mixed solution of ethanol and VO_x sol with a volume ratio of 1:1 for 12 h. Then, the CA filled with VO_x sol was exposed in water vapor at 80°C for 2 h for hydrolysis. V^{4+}-V_2O_5/CA was obtained after being heated at 275°C for 20 min in air.

Structural characterizations

All samples were characterized by means of X-ray powder diffraction (XRD) using a Rigaku D/max-C diffractometer with a Cu Kα radiation source (λ = 1.5406 Å), X-ray photoelectron spectroscopy (XPS, Thermo-VG, Al Kα radiation) and electron paramagnetic resonance (EPR, Bruker BioSpin GmbH). Fourier transform infrared (FTIR) spectroscopy was measured using a Bruker-TENSOR27 within a range from 400 to 4000 cm^{-1}. Thermogravimetric and differential scanning calorimetry (TG-DSC, 10°C min^{-1} at air atmosphere), field emission scanning electron microscopy (SEM, S-4800) and transmission electron microscopy (TEM, HRTEM JEOL-2100) were conducted. Nitrogen adsorption-desorption measurements were carried out to calculate the Brunaue-Emmett-Teller (BET) surface area and pore diameter distribution.

Electrochemical measurements

The electrochemical properties and performance of samples and devices were tested in symmetrical two-electrode configuration with 1 mol L^{-1} Na_2SO_4 aqueous solution as the electrolyte [29]. A slurry prepared by mixing the active materials and poly (vinylidene fluoride) (PVDF) dispersed in *N*-methylpyrrolidone (NMP) at a mass ratio of 9:1 was coated on graphite paper (1 cm × 3 cm) with a mass of about 1 mg and an area of 1 cm^2. Then, these electrodes were dried at 120°C in vacuum for 12 h. The

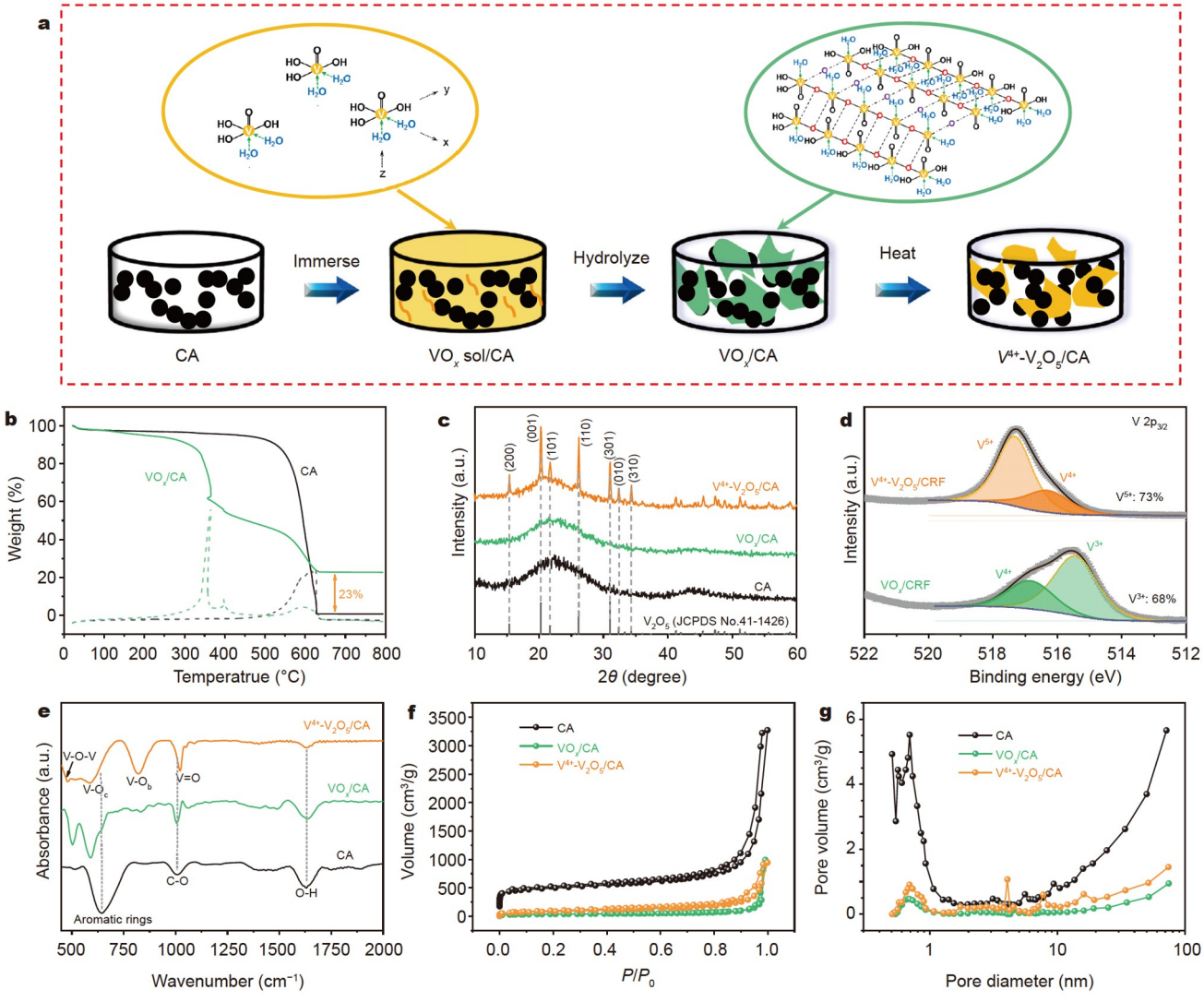

Figure 1 (a) Schematic illustration of the synthesis process of V^{4+}-V_2O_5/CA. (b) TG-DSC curves of VO_x/CA and CA. (c) XRD patterns of CA, VO_x/CA and V^{4+}-V_2O_5/CA. (d) The XPS V $2p_{3/2}$ peaks of VO_x/CA and V^{4+}-V_2O_5/CA. (e) FTIR spectra, (f) nitrogen adsorption-desorption isotherms and (g) pore diameter distributions of CA, VO_x/CA and V^{4+}-V_2O_5/CA.

electrochemical properties of V^{4+}-V_2O_5/CA-based supercapacitors were evaluated by cyclic voltammogram (CV), galvanostatic charge/discharge (GCD), and cycling stability measurements with potential ranging from −1 to 1 V [28,30,31]. Electrochemical impedance spectroscopy (EIS) was collected with a CHI 660C electrochemical workstation in the frequency range from 0.01 to 100 kHz at an alternating current (AC) amplitude of 5 mV. The specific capacitance (C, F g^{-1}), energy density (E, W h kg^{-1}) and power density (P, W kg^{-1}) of a single electrode (C) were calculated respectively by the formulas: $C = 2I\Delta t/\Delta V$, $E = (1/8)C(\Delta V)^2/3600$, and $P = E/\Delta t$, where I is the constant discharging current density, Δt is the discharging time and ΔV is the potential window in the galvanostatic discharge curves [32,33].

RESULTS AND DISCUSSION

Fig. 1a illustrates the fabrication of V^{4+}-V_2O_5/CA nanocomposites. The as-prepared CA was immersed into VO_x sol solution for 12 h, and then exposed in water vapor for 2 h for the hydrolysis process. In VO_x sol, vanadium shows a six-fold coordination with one water molecule and a short V=O double bond along the z axis, another water molecule along x axis and three –OH groups in the equatorial plane. Condensations occurred among H_2O–V–OHs, HO–V–OHs and other –OH groups, forming VO_x in porous CA, namely VO_x/CA. Then, the sample was heat-treated in air to obtain V^{4+}-V_2O_5/CA. TG-DSC measurements were firstly performed to ensure a proper temperature to heat VO_x/CA composites. As shown in Fig. 1b, both CA and VO_x/CA show a tiny weight loss before 120°C, likely due to the removal of adsorbed water. CA was oxidized in air with an exothermic peak at around 600°C and its weight reduces to zero. In contrast, the weight of VO_x/CA reduces slightly between 120 and 200°C probably due to the crystalline water. VO_x/CA shows an appreciable weight loss coupled with a strong exothermic peak at around 350°C, likely attributable to the oxidation of VO_x (amorphous with predominant tetravalent vanadium) and V_2O_5 crystallization. The huge released heat would possibly lead to a local oxidation of CA, resulting in the appreciable weight loss between 200 and 400°C [26]. Then, noncatalyzed oxidization of CA occurs with an exothermic peak at around 600°C. The weight of sample remains 23% after 650°C, which belongs to V_2O_5. Based on above TG-DSC analysis, VO_x/CA was heated at 275°C in air for 20 min to obtain V^{4+}-V_2O_5/CA without overly oxidizing CA.

Fig. 1c displays XRD patterns of VO_x/CA, CA and V^{4+}-V_2O_5/CA; all show two broad bands at around 24° and 44° [15], revealing the presence of amorphous phase in all three samples. CA is amorphous and VO_x in VO_x/CA is also likely amorphous. V^{4+}-V_2O_5/CA displays diffraction peaks that are well indexed to V_2O_5 (JCPDS No.41-1426) in addition to the broad bands of amorphous CA. This result suggests that V^{4+}-V_2O_5/CA is composited with V_2O_5 and CA. Note that the sample contains crystalline V_2O_5 at 275°C, while the crystallization occurs at around 350°C in TG-DSC. It is possible that the real temperature inside the sample is higher than the detected 275°C, which is common for muffle furnace, and hysteresis may occur in TG-DSC measurements. However, it is more likely that amorphous VO_x rich with V^{3+} and V^{4+} catalyze V_2O_5 to crystallize at the interface between VO_x and carbon at lower temperatures with more heat from VO_x oxidation.

Both VO_x/CA and V^{4+}-V_2O_5/CA were further characterized by means of XPS spectroscopy with the results shown in Fig. 1d. Compared with VO_x/CA, the V $2p_{3/2}$ peaks in V^{4+}-V_2O_5/CA shifts to higher binding energy, indicating the vanadium valence increases in V^{4+}-V_2O_5/CA. After deconvolution, the V^{3+} and V^{4+} peaks are presented in VO_x/CA with the percentages of 68% and 32%, respectively. V^{4+}-V_2O_5/CA demonstrates the domination of V^{5+} (73%). The results corroborate that the heat treatment leads to the oxidation of low-valence vanadium and the crystallization of V_2O_5, which agrees well with the reported V_2O_5-coated nanoporous carbon for sodium-ion batteries [26]. The different binding energies of V^{4+} (516.4 and 516.8 eV) indicate that the local chemical surrounding is different from some V^{4+} [34]. The presence of an appreciable amount of V^{4+} (27%) may be caused by the incompletely oxidation of VO_x, and it is also possible that oxygen vacancies are generated as oxygen may be insufficient for the oxidation of VO_x and CA [26]. The average valence of vanadium increases from 3.3 (VO_x/CA) to 4.7 (V^{4+}-V_2O_5/CA) caused by heat treatment. Considering that XPS measurement characterizes the surface of materials (several nanometers), and 27% of V^{4+} in V^{4+}-V_2O_5/CA is surface percentage, it is reasonable that the V^{4+}-V_2O_5/CA exhibits amorphous V_2O_5 phase instead of a mixture of amorphous VO_2 and V_2O_5. Combining XPS and XRD analyses, V^{4+}-V_2O_5/CA consists of V^{4+}-rich V_2O_5 and CA, and the amount of V^{4+} (27%) is notably higher than commonly reported in V_2O_5 (usually less than 10%) [31,35].

FTIR spectra of CA, VO_x/CA and V^{4+}-V_2O_5/CA are shown in Fig. 1e. In the spectrum of CA, peaks at 645, 1004, and 1627 cm^{-1} are assigned to the stretching vibration of aromatic rings, C–O bond and bending vibration of C–H bond in CA, respectively [15]. VO_x/CA shows peaks at 504, 584 and 835 cm^{-1} for V–O–V, V–O_c and V–O_b bonds, and another peak at 1014 cm^{-1} from the overlap of C–O and V=O bonds. The spectrum of V^{4+}-V_2O_5/CA exhibits the characteristic bands of V_2O_5 at 478 cm^{-1} (V–O–V bonds), 586 cm^{-1} (V–O_c bonds), 819 cm^{-1} (V–O_b bonds) and 1022 cm^{-1} (V=O bonds) [36].

In Fig. 1f, the nitrogen adsorption-desorption isotherm curves of CA, VO_x/CA and V^{4+}-V_2O_5/CA exhibit type IV curves with H3 hysteresis loop characteristics according to the IUPAC [12]. In addition, the corresponding pore size distributions (Fig. 1g) suggest a porous structure with micropores, mesopores and macropores in CA, VO_x/CA and V^{4+}-V_2O_5/CA. The porous structure of CA can provide a large contact area for electrolyte and electrodes, shorten the charge transfer distance, and thus facilitate electron transfer and ion diffusion. According to the BET method, the surface area decreases significantly from 1569 (CA) to 125 m^2 g^{-1} (VO_x/CA) because the loading of VO_x takes some space in porous CA. However, the specific surface area increases to 304 m^2 g^{-1} in V^{4+}-V_2O_5/CA likely due to the deposition of small VO_x particles. Compared with VO_x/CA, the larger specific surface area would provide more reactive sites to enhance the charge storage ability of V^{4+}-V_2O_5/CA.

The morphologies of samples are displayed with SEM images. Compared with CA (Fig. 2a–c), curved VO_x nanosheets uniformly disperse among the porous CA in VO_x/CA in Fig. 2d–f. Then, the nanosheets become less curved in V^{4+}-V_2O_5/CA (Fig. 2g–i), which can also result in an increased specific area in V^{4+}-V_2O_5/CA. Further characterized by TEM images (Fig. 2j, k), dark V^{4+}-V_2O_5 nanosheets distribute in CA and the EDS of selected area demonstrates C and V elements in V^{4+}-V_2O_5/CA (Fig. S1). In the HRTEM image of V^{4+}-V_2O_5/CA (Fig. 2l), layered nanosheets were clearly observed with an average distance of

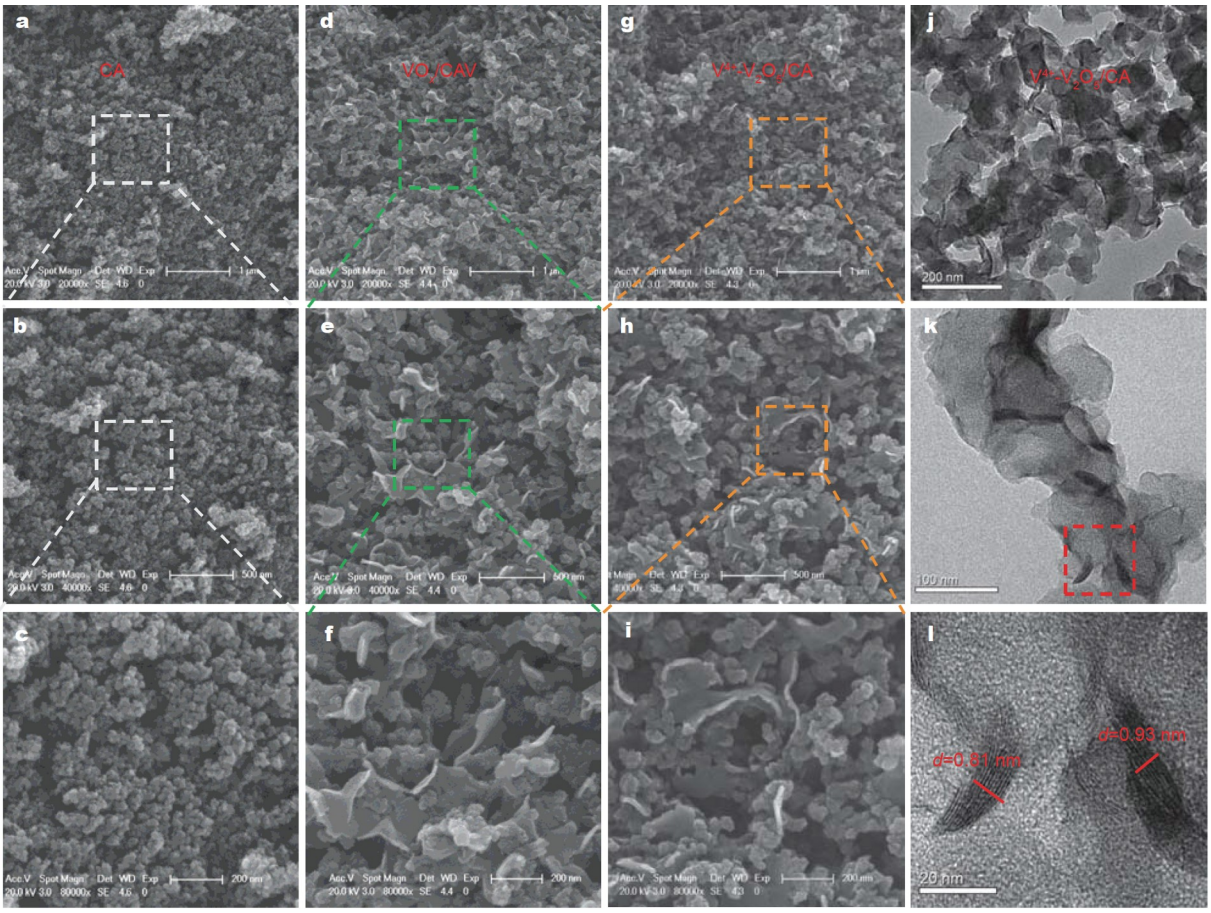

Figure 2 SEM images of (a–c) CA, (d–f) VO_x/CA and (g–i) V^{4+}-V_2O_5/CA. (j–l) TEM and HRTEM images of V^{4+}-V_2O_5/CA.

0.81–0.93 nm. As V^{4+} possesses a larger ionic radius (72 pm) in the six-coordination than V^{5+} (68 pm) in the same surroundings [34], the larger ionic radius of V^{4+} would cause V_2O_5 layer distortions and expand the interlayer distance for fast ion diffusion [36,37]. There is a large fraction of V^{4+} ions in the surface layer, which would affect the interplanar distance and appear uneven, while no peak shift is observed in corresponding XRD pattern. As HRTEM images are highly localized, it is likely that such a deviation occurs in the near surface layer with a small quantity and thus is insensitive to XRD.

The electrochemical properties and performance of CA, VO_x/CA and V^{4+}-V_2O_5/CA were tested in symmetric double-electrode supercapacitors with Na_2SO_4 as electrolyte. As shown in Fig. 3a, all the CV curves of CA, VO_x/CA and V^{4+}-V_2O_5/CA show a nearly rectangle shape at 5 mV s^{-1}, and the CV curves show no obvious distortion as the scan rates increase to 100 mV s^{-1} (Fig. 3b and Fig. S2a, b). In addition, the rectangle area become larger from CA to VO_x/CA and V^{4+}-V_2O_5/CA, indicating an improved specific capacitance due to the loading of V^{4+}-rich V_2O_5 nanosheets. The GCD curves of CA, VO_x/CA and V^{4+}-V_2O_5/CA are presented in Fig. 3c and Fig. S2c, d, respectively. The specific capacitance of V^{4+}-V_2O_5/CA calculated with the GCD curve at 0.5 A g^{-1} (Fig. 3d) is 405 F g^{-1}, much higher than that of VO_x/CA (170 F g^{-1}) and pure CA (123 F g^{-1}). V^{4+}-V_2O_5/CA also exhibits much better rate performance and shows 201 F g^{-1} at a large current density of 10 A g^{-1} (Fig. 3e). Moreover, the energy density of V^{4+}-V_2O_5/CA (56 W h kg^{-1}) is higher than that of VO_x/CA (23 W h kg^{-1}) and CA (17 W h kg^{-1}) when the average power density is 250 W kg^{-1} (Fig. 3f). The above result confirms that V^{4+}-V_2O_5/CA is promising for high-performance supercapacitors. The enhancements in specific capacitance and energy density of V^{4+}-V_2O_5/CA should be attributed to the following factors: (1) In the special nanostructure, the uniformly distribution of V_2O_5 nanosheets in porous CA shortens the electron transfer and ion diffusion distance, and the large specific surface area provides more reaction sites for electrochemical reactions. (2) Crystalline V_2O_5 can make capacitance contributions *via* pseudocapacitive intercalation [38]. High-valence vanadium (V^{5+}) can be reduced to V^{4+} and V^{3+} ($V^{5+} + e^- \rightarrow V^{4+}$, $V^{4+} + e^- \rightarrow V^{3+}$) to store more charges than low-valence vanadium. (3) The accompanied V^{4+} may catalyze the redox reactions and improve the transport kinetics of V^{4+}-V_2O_5/CA, and (4) CA synergistically improves the electrical conductivity and structural integrity.

To study the contributions of V^{4+}, V_2O_5 obtained from the hydrolysis of VO_x and heat-treatment (characterized by XRD and XPS in Fig. S3) was mechanically mixed with CA (noted as V_2O_5/CA) according to the mass ratio from TG results. Tested in the same conditions (Fig. 3g and Fig. S2e, f), the CV curve area of V_2O_5/CA is smaller than that of V^{4+}-V_2O_5/CA. Consistently, the specific capacitance of V_2O_5/CA is 225 F g^{-1} at 0.5 A g^{-1}, larger than that of CA (123 F g^{-1}) and VO_x/CA (170 F g^{-1}). This result confirms that high-valence vanadium (+5) contributes to enhanced specific capacity *via* redox reactions. On the hand, the

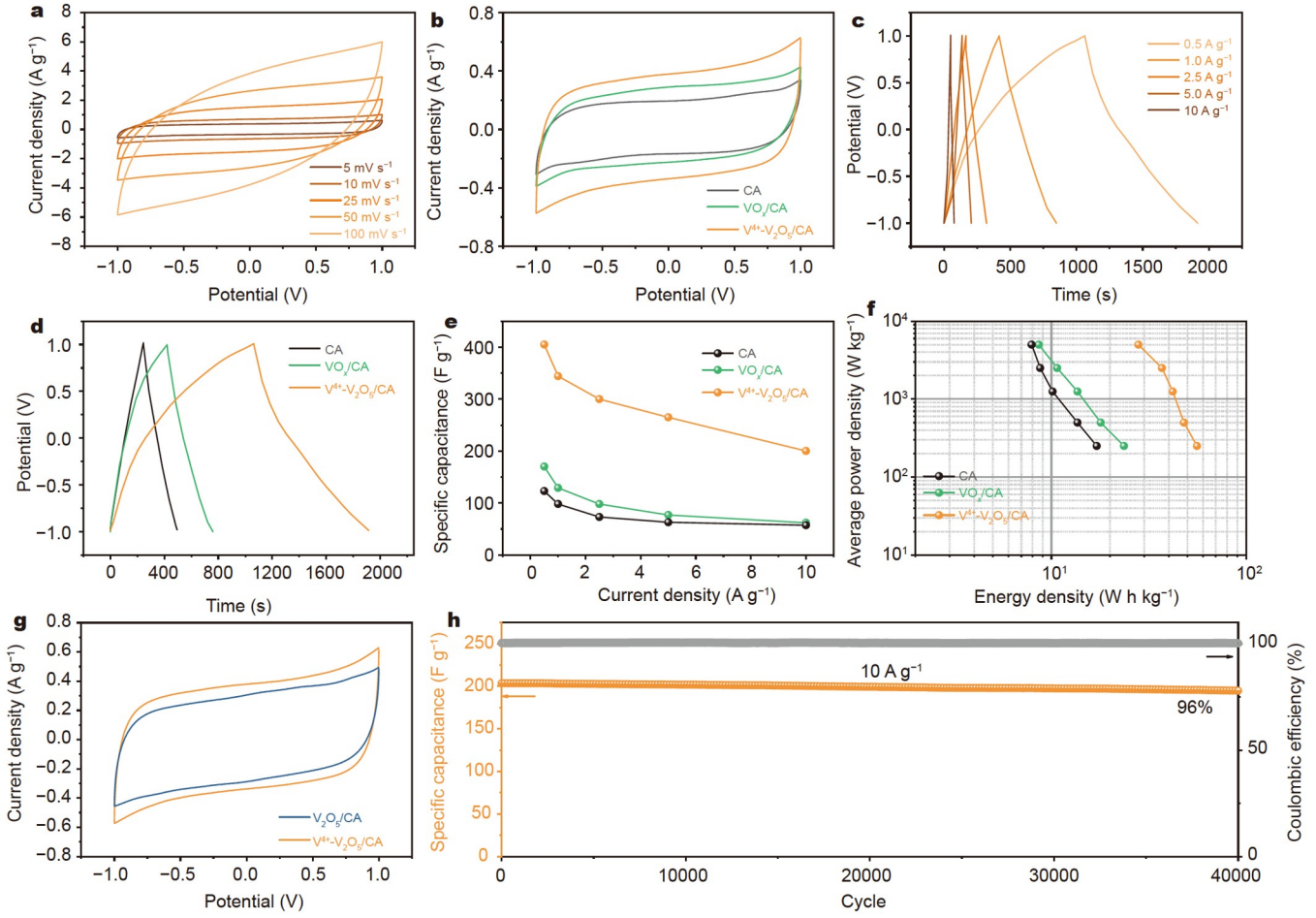

Figure 3 (a) CV curves of V^{4+}-V_2O_5/CA at different scan rates. (b) CV curves of CA, VO_x/CA and V^{4+}-V_2O_5/CA at 5 mV s^{-1}. (c) GCD curves of V^{4+}-V_2O_5/CA at different current densities. (d) GCD curves of CA, VO_x/CA and V^{4+}-V_2O_5/CA at 0.5 A g^{-1}. (e) Specific capacitances tested at different current densities, and (f) Ragone plots of CA, VO_x/CA and V^{4+}-V_2O_5/CA. (g) CV curves of V^{4+}-V_2O_5/CA and V_2O_5/CA at 5 mV s^{-1}. (h) Cycling performance of V^{4+}-V_2O_5/CA at 10 A g^{-1}.

specific capacitance of V_2O_5/CA (225 F g^{-1}) is nearly half that of V^{4+}-V_2O_5/CA (405 F g^{-1}), indicating the capacitance contribution of V^{4+}. The accompanied V^{4+} may catalyze the redox reactions and improve the transport kinetics of V^{4+}-V_2O_5/CA, as reported in self-doped V^{4+}-V_2O_5 nanoflakes [27]. Density functional theory calculations suggest that the density of states of V^{4+} is different from that of V^{5+}. As the electrons occupy V 3d orbitals at the conduction band bottom of V^{4+}, V^{4+} thus improves the electrical conductivity of electrodes, which catalyzes the redox reactions and improves the transport kinetics [39].

V^{4+}-V_2O_5/CA also demonstrates excellent cycling performance. As shown in Fig. 3h, the initial capacitance is 201 F g^{-1} at 10 A g^{-1}, and 96% is maintained after 40,000 charge/discharge processes. However, only 62% retention is kept in VO_x/CA after 20,000 cycles (Fig. S4). CA exhibits superior stability of 95% capacitance retention after 20,000 cycles, but the initial capacitance is as low as 57 F g^{-1} (Fig. S4). The long lifespan of V^{4+}-V_2O_5/CA is attributed to CA which stabilizes the structure with a firm and conductive framework. Also, V^{4+} also helps to improve the stability of V_2O_5 nanosheets with fast charge transportation. Moreover, the cycling performance of V^{4+}-V_2O_5/CA is also better than those of other materials, such as V_2O_5/graphene/CNT (82.9% capacitance retention after 32,500 cycles at 10 A g^{-1}) [40], Co_2VO_4 (87% capacitance retention after 18,000 cycles at 10 A g^{-1}) [3], and N,S self-doped hollow-sphere porous carbon (80.3% capacitance retention after 5000 cycles at 5 A g^{-1}) [41].

The kinetic factors for the excellent electrochemical performance of V^{4+}-V_2O_5/CA were explored with EIS measurements. As shown in Nyquist plots in Fig. 4a, the Z'-intercept, the semicircle and the sloping line correspond to the internal resistance mostly from internal resistance (R_s), charge transfer resistance (R_{ct}) at the electrode/electrolyte interface and ion diffusion of the electrode, respectively. In this work, the almost same R_s values suggest less effects from the system. The smaller R_{ct} value and steeper slope of V^{4+}-V_2O_5/CA than CA and VO_x/CA (Fig. 4b) suggest that electron transfer and ion diffusion kinetics are enhanced by V^{4+}-rich V_2O_5 nanosheets. In addition, the ion diffusion coefficient (D_n) can be calculated with the following equation [8]:

$$D_n = R^2T^2/(2A^2n^4F^4C^2\sigma^2), \quad (1)$$

where R (gas constant), T (absolute temperature), A (surface area of electrode), n (the number of transferred electrons), F (Faraday constant) and C (the concentration of ions) are constant. Warburg factor (σ) can be obtained by fitting the low-

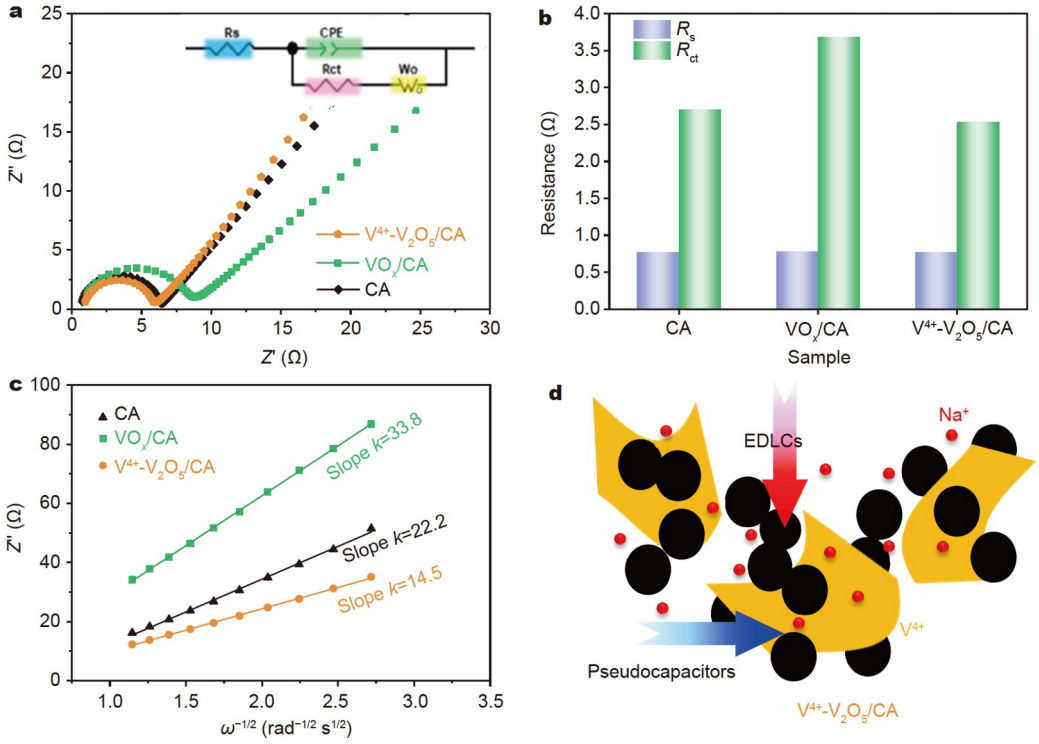

Figure 4 (a) Nyquist plots and equivalent circuit model. (b) R_s and R_{ct} values of CA, VO_x/CA and V^{4+}-V_2O_5/CA from the corresponding Nyquist plots. (c) The relationship between the real part of impedance and low frequencies. The smaller slope of the linear tendency indicates faster ion diffusion. (d) The schematic diagram of charge storage mechanism of V^{4+}-V_2O_5/CA.

frequency points as Z'' *vs.* $\omega^{-1/2}$, where ω is the angular frequency (Fig. 4c). As calculated, D_n of V^{4+}-V_2O_5/CA, CA and VO_x/CA are 2.7×10^{-10}, 1.1×10^{-10} and 5.0×10^{-11} cm^2 s^{-1}, respectively. The results indicate that the transport kinetics is greatly enhanced in V^{4+}-V_2O_5/CA. Coherent nanocomposite structure and components collectively made noticeable enhancements in electrochemical properties and supercapacitor performance. As illustrated in Fig. 4d, the porous CA used as an EDLC electrode material stores charges by adsorption/desorption of charges with a large specific surface area [13,41]. Moreover, V_2O_5 nanosheets show pseudo-capacitive reactions although there are no obvious redox peaks in CV curves [38,42]. In addition, the V_2O_5 nanosheets uniformly distribute in porous CA in V^{4+}-V_2O_5/CA. The electron transfer and ion diffusion distance are shortened, thus facilitating charge transportation and enhancing charge kinetics. The large specific surface area of V^{4+}-V_2O_5/CA composite also provides a large amount of reaction sites for surface adsorption/desorption and pseudo-capacitive reactions.

CONCLUSIONS

Direct hydrolysis and condensation of VO_x sol in porous CA is demonstrated to be an effective approach in the synthesis of V^{4+}-rich V_2O_5/CA. The uniform distribution of V_2O_5 nanosheets shortens the charge transfer pathway with more reactive sites for redox reactions. V^{4+} is believed to enhance the transport kinetics of V^{4+}-V_2O_5/CA and catalyze the electrochemical reactions. V^{4+}-V_2O_5/CA achieves a high specific capacitance of 405 F g^{-1} and exhibits a long lifespan (96% capacitance remained after 40,000 cycles). The excellent electrochemical properties and supercapacitor performance of V^{4+}-V_2O_5/CA are attributed to the combined contribution of coherent nanocomposite structure and the presence of crystalline V_2O_5 nanosheets with a large amount of V^{4+}.

Received 3 November 2021; accepted 22 December 2021; published online 4 March 2022

1 Chu S, Majumdar A. Opportunities and challenges for a sustainable energy future. Nature, 2012, 488: 294–303
2 Wang G, Zhang L, Zhang J. A review of electrode materials for electrochemical supercapacitors. Chem Soc Rev, 2012, 41: 797–828
3 Yuan F, Gao G, Jiang X, *et al.* Suppressing the metal-metal interaction by $CoZn_{0.5}V_{1.5}O_4$ derived from two-dimensional metal-organic frameworks for supercapacitors. Sci China Mater, 2022, 65: 105–114
4 Wang Y, Yuan H, Zhu Y, *et al.* An all-in-one supercapacitor working at sub-zero temperatures. Sci China Mater, 2020, 63: 660–666
5 Miller JR, Simon P. electrochemical capacitors for energy management. Science, 2008, 321: 651–652
6 Wang Y, Song Y, Xia Y. Electrochemical capacitors: Mechanism, materials, systems, characterization and applications. Chem Soc Rev, 2016, 45: 5925–5950
7 Miao C, Zhou C, Wang HE, *et al.* Hollow Co–Mo–Se nanosheet arrays derived from metal-organic framework for high-performance supercapacitors. J Power Sources, 2021, 490: 229532
8 Bi W, Wang J, Jahrman EP, *et al.* Interface engineering V_2O_5 nanofibers for high-energy and durable supercapacitors. Small, 2019, 15: 1901747
9 Ren J, Shen M, Li Z, *et al.* Towards high-performance all-solid-state asymmetric supercapacitors: A hierarchical doughnut-like Ni_3S_2@PPy core–shell heterostructure on nickel foam electrode and density functional theory calculations. J Power Sources, 2021, 501: 230003
10 Simon P, Gogotsi Y. Materials for electrochemical capacitors. Nat Mater, 2008, 7: 845–854
11 Jiang H, Lee PS, Li C. 3D carbon based nanostructures for advanced supercapacitors. Energy Environ Sci, 2013, 6: 41–53

12 Rauda IE, Augustyn V, Saldarriaga-Lopez LC, *et al.* Nanostructured pseudocapacitors based on atomic layer deposition of V_2O_5 onto conductive nanocrystal-based mesoporous ITO scaffolds. Adv Funct Mater, 2014, 24: 6717–6728
13 Biener J, Stadermann M, Suss M, *et al.* Advanced carbon aerogels for energy applications. Energy Environ Sci, 2011, 4: 656–667
14 Chien HC, Cheng WY, Wang YH, *et al.* Ultrahigh specific capacitances for supercapacitors achieved by nickel cobaltite/carbon aerogel composites. Adv Funct Mater, 2012, 22: 5038–5043
15 Yamada H, Nakamura H, Nakahara F, *et al.* Electrochemical study of high electrochemical double layer capacitance of ordered porous carbons with both meso/macropores and micropores. J Phys Chem C, 2007, 111: 227–233
16 Pan A, Liu D, Zhou X, *et al.* Enhanced lithium-ion intercalation properties of coherent hydrous vanadium pentoxide–carbon cryogel nanocomposites. J Power Sources, 2010, 195: 3893–3899
17 Li J, Wang X, Huang Q, *et al.* Studies on preparation and performances of carbon aerogel electrodes for the application of supercapacitor. J Power Sources, 2006, 158: 784–788
18 Jiang J, Li Y, Liu J, *et al.* Recent advances in metal oxide-based electrode architecture design for electrochemical energy storage. Adv Mater, 2012, 24: 5166–5180
19 Béguin F, Presser V, Balducci A, *et al.* Carbons and electrolytes for advanced supercapacitors. Adv Mater, 2014, 26: 2219–2251
20 Wu C, Feng F, Xie Y. Design of vanadium oxide structures with controllable electrical properties for energy applications. Chem Soc Rev, 2013, 42: 5157–5183
21 Perera SD, Liyanage AD, Nijem N, *et al.* Vanadium oxide nanowire—graphene binder free nanocomposite paper electrodes for supercapacitors: A facile green approach. J Power Sources, 2013, 230: 130–137
22 Chandrappa GT, Steunou N, Cassaignon S, *et al.* Hydrothermal synthesis of vanadium oxide nanotubes from V_2O_5 gels. Catal Today, 2003, 78: 85–89
23 Qu QT, Shi Y, Li LL, *et al.* $V_2O_5{\cdot}0.6H_2O$ nanoribbons as cathode material for asymmetric supercapacitor in K_2SO_4 solution. Electrochem Commun, 2009, 11: 1325–1328
24 Yan Y, Li B, Guo W, *et al.* Vanadium based materials as electrode materials for high performance supercapacitors. J Power Sources, 2016, 329: 148–169
25 Saravanakumar B, Purushothaman KK, Muralidharan G. Interconnected V_2O_5 nanoporous network for high-performance supercapacitors. ACS Appl Mater Interfaces, 2012, 4: 4484–4490
26 Raju V, Rains J, Gates C, *et al.* Superior cathode of sodium-ion batteries: Orthorhombic V_2O_5 nanoparticles generated in nanoporous carbon by ambient hydrolysis deposition. Nano Lett, 2014, 14: 4119–4124
27 Song H, Liu C, Zhang C, *et al.* Self-doped V^{4+}–V_2O_5 nanoflake for 2 Li-ion intercalation with enhanced rate and cycling performance. Nano Energy, 2016, 22: 1–10
28 Wu Y, Gao G, Wu G. Self-assembled three-dimensional hierarchical porous V_2O_5/graphene hybrid aerogels for supercapacitors with high energy density and long cycle life. J Mater Chem A, 2015, 3: 1828–1832
29 Stoller MD, Ruoff RS. Best practice methods for determining an electrode material's performance for ultracapacitors. Energy Environ Sci, 2010, 3: 1294
30 Zhu J, Cao L, Wu Y, *et al.* Building 3D structures of vanadium pentoxide nanosheets and application as electrodes in supercapacitors. Nano Lett, 2013, 13: 5408–5413
31 Wu Y, Gao G, Yang H, *et al.* Controlled synthesis of V_2O_5/MWCNT core/shell hybrid aerogels through a mixed growth and self-assembly methodology for supercapacitors with high capacitance and ultralong cycle life. J Mater Chem A, 2015, 3: 15692–15699
32 Wang X, Zhang Y, Zhi C, *et al.* Three-dimensional strutted graphene grown by substrate-free sugar blowing for high-power-density supercapacitors. Nat Commun, 2013, 4: 2905
33 Yang X, Cheng C, Wang Y, *et al.* Liquid-mediated dense integration of graphene materials for compact capacitive energy storage. Science, 2013, 341: 534–537
34 Liu C, Neale Z, Zheng J, *et al.* Expanded hydrated vanadate for high-performance aqueous zinc-ion batteries. Energy Environ Sci, 2019, 12: 2273–2285
35 Bi W, Wu Y, Liu C, *et al.* Gradient oxygen vacancies in V_2O_5/PEDOT nanocables for high-performance supercapacitors. ACS Appl Energy Mater, 2018, 2: 668–677
36 Bi W, Jahrman E, Seidler G, *et al.* Tailoring energy and power density through controlling the concentration of oxygen vacancies in V_2O_5/PEDOT nanocable-based supercapacitors. ACS Appl Mater Interfaces, 2019, 11: 16647–16655
37 Bi W, Gao G, Wu G, *et al.* Sodium vanadate/PEDOT nanocables rich with oxygen vacancies for high energy conversion efficiency zinc ion batteries. Energy Storage Mater, 2021, 40: 209–218
38 Zhang Q, Levi MD, Dou Q, *et al.* The charge storage mechanisms of 2D cation-intercalated manganese oxide in different electrolytes. Adv Energy Mater, 2019, 9: 1802707
39 Liu C, Tian M, Wang M, *et al.* Catalyzing zinc-ion intercalation in hydrated vanadates for aqueous zinc-ion batteries. J Mater Chem A, 2020, 8: 7713–7723
40 Bi W, Gao G, Wu Y, *et al.* Novel three-dimensional island-chain structured V_2O_5/graphene/MWCNT hybrid aerogels for supercapacitors with ultralong cycle life. RSC Adv, 2017, 7: 7179–7187
41 Shang M, Zhang J, Liu X, *et al.* N, S self-doped hollow-sphere porous carbon derived from puffball spores for high performance supercapacitors. Appl Surf Sci, 2021, 542: 148697
42 Wang JG, Liu H, Liu H, *et al.* Interfacial constructing flexible V_2O_5@polypyrrole core–shell nanowire membrane with superior supercapacitive performance. ACS Appl Mater Interfaces, 2018, 10: 18816–18823

Acknowledgements The authors acknowledge the support from the National Natural Science Foundation of China (51872204, 52072261, and 22011540379), Shanghai Sailing Program (21YF1430900), the National Key Research and Development Program of China (2017YFA0204600) and Shanghai Social Development Science and Technology Project (20dz1201800). This work is also supported by the National Natural Science Foundation (1803256). The authors are grateful to the Deanship of the Scientific Research, King Saud University for funding through Vice Deanship of Scientific Research Chairs.

Author contributions Bi W designed and performed the experiment, analyzed the data, and wrote and revised the manuscript. Deng S, Tang H, Liu Y, Shen J, Gao G, Wu G, Atif M and AlSalhi M helped with the experiment. Cao G contributed to the theoretical analysis and manuscript revision. All authors contributed to the general discussion.

Conflict of interest The authors declare no conflict of interest.

Supplementary information Supporting data are available in the online version of the paper.

Wenchao Bi received her PhD degree in physics from Tongji University in 2020. She was a joint PhD candidate of the University of Washington (Seattle) in 2017–2019. She joined the Departments of Physics, College of Science, University of Shanghai for Science and Technology in 2020. Her research focuses on electrode material design and energy storage mechanism exploration of zinc ion batteries and supercapacitors.

Guohua Gao is an associate professor at the School of Physical Science and Engineering, Tongji University. He obtained his PhD degree in materials physics and chemistry from Tongji University in 2010. His main research interests focus on energy storage and conversion, first principles, and vanadium-based nanohybrids.

Guangming Wu is a professor at the School of Physical Science and Engineering, Tongji University. He obtained his PhD degree in condensed matter physics from Tongji University in 1998. His main research interests focus on functional nanomaterials, artificial regulation of micro-nano structure, energy storage and energy saving.

Guozhong Cao is a Boeing-Steiner professor of materials science and engineering, professor of chemical engineering and adjunct professor of mechanical engineering at the University of Washington, Seattle. He received his BSc degree from East China University of Science and Technology, MSc degree from Shanghai Institute of Ceramics, Chinese Academy of Sciences, and PhD from Eindhoven University of Technology, the Netherlands.

富含V^{4+}的V_2O_5/碳气凝胶纳米复合材料用于高性能超级电容器

毕文超[1,2,3], 邓声远[2], 汤海莎[1], 刘源[1], 沈军[2], 高国华[2*], 吴广明[2*], M. Atif[4,5], MS AlSalhi[4,5], 曹国忠[3*]

摘要 本文利用原位水解-聚合的方法合成了富含V^{4+}的V_2O_5/碳气凝胶纳米复合材料(V^{4+}-V_2O_5/CA), 用于超级电容器的电极. 在合成过程中, 碳气凝胶(CA)促进了无序氧化钒的沉积并催化富含V^{4+}的V_2O_5在较低的温度下结晶. 由于V_2O_5纳米片均匀地分布在CA内, 这种特殊结构为电化学储能反应提供了大比表面积和更多的活性位点; CA协同提高了电极材料的导电性和结构稳定性; 丰富的V^{4+}增强了V_2O_5原有的导电性、促进了离子扩散速率并催化了电化学反应. 因此, 基于V^{4+}-V_2O_5/CA的超级电容器获得了高比容量(在0.5 A g^{-1}下比容量达405 F g^{-1})、高能量密度(56 W h kg^{-1}, 功率密度为 250 W kg^{-1}) 和长循环寿命(40,000次循环后比容量保持率为96%).